Nanoscale

PAPER

View Article Online
View Journal | View Issue

Cite this: *Nanoscale*, 2025, **17**, 23000

Impact of high oxygen deficiency on the photoluminescence properties of black zinc oxide thin films

Magdalena Nistor, *[a] Daniela Dobrin, [a] Florin Gherendi [a] and Jacques Perrière[b,c]

The presence of oxygen deficiency in ZnO thin films is a key factor for tailoring their optical and electrical properties. Highly oxygen-deficient zinc oxide thin films were synthesized by pulsed electron beam deposition and investigated by Rutherford backscattering spectrometry, photoluminescence, X-ray diffraction, Hall effect measurements, and X-ray photoelectron spectroscopy. At a high degree of deficiency of about 15%, leading to black (or dark) films, zinc oxide films were found to be amorphous. The optical properties are dominated by the introduction of deep-level defect states that absorb visible light, whereas the electrical properties are governed by the increased electron concentration in the conduction band (6.55×10^{20} cm^{-3}). These oxygen-deficient zinc oxide films exhibited enhanced violet and blue photoluminescence emission in the range of 408–456 nm, attributed to zinc interstitials and their extended states.

Received 12th May 2025,
Accepted 2nd September 2025

DOI: 10.1039/d5nr01937k

rsc.li/nanoscale

A. Introduction

Nanocomposite thin films consisting of metal nanoclusters embedded in an oxide matrix have attracted increasing attention, due to their novel physical and chemical properties obtained from their nano-scale size, for promising applications in areas of optoelectronic materials and devices, energy conversion, energy storage, catalysis, environmental science, and biomedicine.[1,2] Among oxide candidates, zinc oxide (ZnO) allows versatile growth in various nanoscale forms and presents a rich defect chemistry.[3] ZnO is a semiconductor oxide with a wide range of applications in optoelectronic devices, sensors, and transparent electronics due to its high exciton binding energy (~60 meV), wide bandgap (~3.37 eV), versatile electrical properties, and piezoelectric characteristics. However, defects in ZnO thin films and nanostructures significantly influence their optical, electrical, and structural properties.[3] Understanding the impact of oxygen deficiency on the composition, properties, and native defect formation of ZnO thin films is crucial for tailoring the material properties for specific applications.

Oxygen deficiency in ZnO usually occurs from an imbalance between zinc and oxygen during growth. Although the predominant ionic defects are Zn interstitials and oxygen vacancies, which are defects that dominate native ZnO, these defects remain a subject for debate.[3] Both defects donate two electrons; therefore, distinguishing one from the other is challenging using only electrical measurements but their photoluminescence signatures could improve the understanding.

As the degree of oxygen deficiency in the ZnO thin films increases, the films change from transparent or slightly yellowish to a progressively darker color. When ZnO (film or bulk) has a high level of oxygen deficiency, it turns black (or dark) in appearance.[4–11] This change is primarily due to the formation of defects within the bandgap, causing the ZnO to absorb light in the visible spectrum. At high concentrations of defects, the quenching of the excitonic luminescence of ZnO leads to the formation of photoluminescence bands, particularly in the ultraviolet and blue regions,[12–16] which are less common than those in the visible region.[17] The electronic structure is also modified, leading to an increased concentration of free carriers (electrons) in the films. This often results in enhanced electrical conductivity, with the films exhibiting n-type behavior, which can be advantageous for certain applications that do not require optical transparency.[11–16]

Several attempts were made to grow black ZnO films and nanostructures either by chemical methods (physicochemical reduction in solution,[5] electrochemical oxidation of Zn foil,[6,7] sol–gel method,[8] and anodic oxidation of metallic zinc[9,10]) or physical methods (pulsed electron beam deposition,[11] pulsed laser deposition[18] and magnetron sputtering[4]). Most of these black or dark ZnO films have the Zn metallic phase inside the oxide matrix, being nanocomposite thin films, but only a few studies have quantitatively measured oxygen deficiency in black ZnO films.[18]

[a]*National Institute for Lasers, Plasma and Radiation Physics (NILPRP), L22 P.O. Box. MG-36, 77125 Bucharest, Magurele, Romania. E-mail: magda.nistor@inflpr.ro*
[b]*Sorbonne Universités, UPMC Univ Paris 06, UMR 7588, INSP, F-75005 Paris, France*
[c]*CNRS, UMR 7588, INSP, F-75005 Paris, France*

Zinc oxide was difficult to obtain in amorphous form in thin films, knowing that crystallization of the film in the hexagonal würtzite (*P*63*mc*) structure occurs easily close to room temperature on different substrates, in particular, on single crystalline c-cut sapphire.[19,20] Previous efforts have mostly been focused on growing amorphous transparent ZnO thin films at cryogenic temperatures using pulsed laser deposition and sputtering[21–23] or in chemical solutions.[24,25] The advantages of amorphous ZnO as an interfacial structure in the suppression of dendrite growth and parasitic reactions of zinc metal anodes in aqueous media were demonstrated for zinc metal batteries.[26] These are an alternative to rechargeable lithium-ion batteries due to their low cost, safety and good electrochemical performance. Amorphous ZnO showed moderate adsorption energy, strong desolvation ability, and hydrophilicity, improving the cycling and thus eliminating the main concerns of these batteries related to safety, capacity degradation and unsatisfactory cycle life.[26,27] Amorphous ZnO on the Zn metal presented a disordered microstructure, good conductivity and the lack of a grain boundary that effectively homogenized the distribution of ions and electrons at the electrode interface.[28] Recently, high oxygen deficiency in ZnO emerged as a promising strategy for amorphous black ZnO thin films with enhanced absorption in the visible and near-infrared regions.[11]

Although photoluminescence spectroscopy[12–17,29,30] and Hall effect measurements[20,31,32] have been widely used to characterize the crystalline ZnO films, amorphous ZnO thin films with high oxygen deficiency have been less studied by these methods. On the other hand, Zn rich ZnO thin films and nanostructures grown using non-equilibrium methods often exhibit lower photoluminescence efficiency due to the lack of long-range order and are more susceptible to defect-related emissions.[12–16] In contrast, epitaxial ZnO thin films, which are grown with well-defined crystallographic alignment to a substrate, exhibit high crystallinity[33–35] and are typically associated with superior optical properties and an intense excitonic peak in photoluminescence spectra.[17,29,30]

In this work, high oxygen deficient amorphous ZnO thin films were grown by pulsed electron beam deposition (PED), a non-equilibrium method[2,11,20,36–41] that has features in common with pulsed laser deposition[18,19,21,33–35] to grow either epitaxial[20,36,39] or nanocomposite thin films.[2,36] The physical properties of highly oxygen deficient and amorphous ZnO thin films were investigated by combining photoluminescence spectroscopy, Rutherford backscattering spectrometry, X-ray diffraction, Hall measurements and X-ray photoelectron spectroscopy. Additionally, we discuss how high oxygen deficiency impacts the optical and electrical properties, offering a more complete understanding of the behavior and performance of black amorphous ZnO thin films that may enable a combination of very distinct properties for novel applications.

B. Experimental

Oxygen deficient ZnO_x thin films were grown by PED on c-cut single crystalline sapphire substrates (CrysTec GmbH) at a temperature of 300 °C in argon at a pressure of 9×10^{-3} mbar. The PED setup and the working concept have been described previously.[2,11,20,38] The pulsed electron beam of about 100 ns FWHM interacts with the ceramic ZnO target at 45°, generating an ablation plasma that mediates the growth of the films on a substrate located parallel to the target at 4 cm. The following growth parameters were used: 15 kV high voltage, 16 nF external capacitor and a repetition rate of about 1 Hz. Argon was selected as the background gas to prevent chemical reactions that could affect the results.

In contrast to pulsed laser deposition, the PED method is used for thin film deposition within a narrow window of working pressure, situated around 10^{-2} mbar, within which the generation and propagation towards the target of the pulsed electron beam occur simultaneously.[38]

Photoluminescence measurements (PL) of ZnO thin films were carried out at room temperature with a FLS 920 Edinburgh Instruments spectrofluorometer equipped with a 450 W Xe lamp excitation source and double monochromators on both excitation and emission using an excitation wavelength of 350 nm.

Rutherford backscattering spectrometry (RBS) was performed using the 2 MeV Van de Graaff accelerator at INSP, Sorbonne Université, to determine the composition and thickness of the ZnO thin films grown by PED.

X-ray photoelectron spectroscopy (XPS) of films was carried out with the help of a Thermo Scientific ESCALAB Xi+ spectrometer at NILPRP. The survey and high-resolution spectra (Zn 2p, Zn 3p, Zn LMM, O 1s, and C 1s) were recorded with a pass energy of 100 eV and an energy step size of 1 eV for the survey spectra and a pass energy of 20 eV and an energy step size of 0.1 eV for the high-resolution spectra, using a monochromatic Al Kα (1486.6 eV) X-ray source. The etching of the film surface was done for 60 s using a 2 keV argon ion beam and the electron flood source was used to compensate for the electrical charging. The Thermo Scientific Avantage software was used for the interpretation of spectra.

The phase structure was investigated using X-ray diffraction (XRD) patterns recorded using a Philips Xpert MRD diffractometer with the Cu Kα radiation (λ = 0.154 nm).

The resistivity, mobility and density of charge carriers were measured using the Van der Pauw and Hall methods in an MMR Technologies, Inc. setup.

C. Results and discussion

Accurately measuring the composition of ZnO thin films, especially the oxygen content, is essential for understanding and controlling their optical and electrical properties.[19,38] The composition and thickness of the black zinc oxide were obtained for the ZnO_x thin films grown by PED on c-cut single crystalline sapphire substrates at a temperature of 300 °C in argon at a pressure of 9×10^{-3} mbar by means of fitted RBS spectra (Fig. 1a) using the RUMP (Rutherford Universal Manipulation Program).[42] In this software, the stoichiometry and thickness are determined from the best-fit by comparing

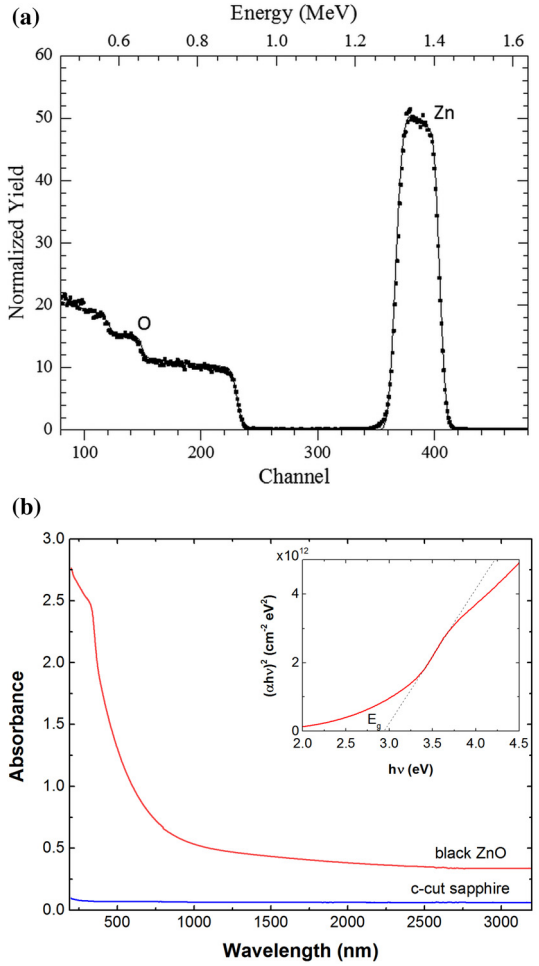

Fig. 1 (a) Experimental RBS spectrum (squares) and the fit of the spectrum (line) and (b) absorption spectrum of a black ZnO_x thin film grown by PED on a c-cut single crystal sapphire substrate at 300 °C in argon at a pressure of 9×10^{-3} mbar. The inset shows the Tauc plot.

the experimental RBS spectrum with the simulated one based on theoretical calculations of Rutherford scattering and energy loss of ions in matter. A thickness of 96 nm and a 15% oxygen deficiency ($ZnO_{0.85}$) in the limits of the 4% precision of the RBS analysis for oxygen were deduced from the fitting of the RBS data in the RUMP software, where a two-layer model of the ZnO_x thin film and sapphire substrate was considered. When the Zn_1O_1 stoichiometry was taken into account in the film, the experimental spectrum was not properly fitted; thus, the data were iteratively fitted until the best fit spectrum (line) was obtained, which was for $Zn_1O_{0.85}$ (Fig. 1a). The fitted RBS spectrum does not show the presence of other impurities in the film. The film oxygen deficiency is preserved throughout the thickness of the film. Moreover, an analysis was conducted by RBS at one-year intervals, and it was found that the composition of $ZnO_{0.85}$ remained constant. This indicates that the films exhibit remarkable stability under ambient conditions.

In addition, X-ray photoelectron spectroscopy (XPS) was performed and the survey spectrum did not reveal impurities in the films.

A high level of oxygen deficiency in ZnO (in the film or bulk form) results in a black or dark appearance.[4–11] A typical example of the absorbance spectrum for a $Zn_1O_{0.85}$ thin film is given in Fig. 1b, showing that the absorption in the visible and near-infrared regions is considerable and associated with the black (dark) color of these thin films. The Tauc plot (inset of Fig. 1b) of a black $ZnO_{0.85}$ film yielded a bandgap of 2.95 eV, similar to other reports,[5,11] while grey-colored films presented typically bandgap values ranging from 3.09 to 3.18 eV.[4] These values differ from the commonly reported bandgap values for transparent, crystalline, and stoichiometric ZnO (3.2–3.37 eV [3,5]). The narrow band gap is due to a large oxygen deficiency in the film,[5,9,10,43] which generates subgap states, as shown by theoretical calculations for In_2O_x.[43]

In PED, the control of the oxygen incorporation in ZnO_x thin films depends on the growth parameters, the gas pressure and the energy of the species emitted by the target.[20,36] The pulsed electron beam ablation of the ZnO target provides high kinetic energy (tens of eV) to the Zn and O atoms in the plasma plume.[40] Like in PLD, several possible sources of oxygen (the target, background gas, and substrate) can contribute to the oxidation process during pulsed laser deposition of oxide thin films.[44,45] As in PLD, approximately 45% of the oxygen in the film originates from the background gas, while the difference is directly incorporated from the target. Furthermore, oxygen is only incorporated in the films during the growth period (*i.e.* during the pulse of the electron beam), while oxidation and oxygen exchange do not occur between successive beam pulses[44] and the oxygen release from the sapphire substrate is mostly negligible.[45]

A more generalized numerical modeling of the plasma plume propagation and oxidation during pulsed laser deposition of TiO_2 thin films showed that the oxidation state of the arriving particles (Ti, TiO, and TiO_2) on the substrate surface depends on the oxygen background pressure.[45] At low oxygen pressure of about 2×10^{-2} mbar, fast oxygen atoms arrive prior to the slower titanium atoms, impacting the oxidation state of the initial substrate surface.[45] Due to the similarities between PED and PLD propagation plume for ZnO at similar pressures at 10^{-2} mbar,[40,44] numerical simulations[45] and angular distribution of complex oxides containing elements with different mass ratios,[38] the oxygen atoms arrive faster and prior to the slower, heavier, zinc atoms in argon background gas. Therefore, the PED growth in argon at 10^{-2} mbar pressure (few collisions[38]) with high kinetic energies of the target species will contribute to zinc oxide thin films with large oxygen deficiency.

A typical photoluminescence (PL) spectrum of ZnO thin films consists of two main regions: (i) the near-band-edge (NBE) emission, which is attributed to the recombination of free excitons, and (ii) defect-related emissions, which occur at lower energies and are often associated with deep-level defects such as oxygen vacancies, zinc interstitials, or dopants in the film.[17,46–51]

Photoluminescence measurements at room temperature were performed on $ZnO_{0.85}$ thin films with an excitation wave-

length of 350 nm. The photoluminescence spectrum of a $ZnO_{0.85}$ thin film is shown in Fig. 2. The overall shape of the PL spectrum is related to the large oxygen deficiency that introduces defect-related emissions at energies lower than the bandgap.[46–51]

The PL spectrum consists of a weak and broadened NBE emission at 3.3 eV and intense defect-related emission bands in the region of 2.2–3.2 eV. The peaks located at 408, 432 and 456 nm correspond to 3.0, 2.9 and 2.7 eV. All peaks were fitted with four Gaussian curves (Fig. 2).[12,13] A notable reduction in the intensity of the ultraviolet emission at 3.3 eV is observed, which is explained by the formation of defects in the films that provide additional channels for electron–hole recombination.

Defect-related emission bands in the visible range, centered at ~2.2 eV (green emission) and commonly associated with oxygen vacancies acting as deep-level defects within the ZnO bandgap,[17,47] are not observed in Fig. 2.

The PL peaks observed between 2.7 and 2.9 eV are attributed to the violet and blue luminescence, primarily associated with the presence of zinc interstitials (Zn_i) and extended Zn_i states, which represent a native defect in the crystal structure of zinc oxide.[12–16,46–51] Zn_i are donor-type defects that introduce additional energy levels into the band gap of ZnO, enabling electronic transitions that lead to the emission of light when the material is excited with ultraviolet photons.[3,12–16]

The violet and blue luminescence is less often observed but occurs in zinc-rich ZnO samples obtained under non-equilibrium synthesis conditions.[12–16,46–51] A study by Zhang *et al.*[12] reported that the assignment of this PL band to Zn_i is supported by the Zn-excess in as-synthesized ZnO smoke samples (Zn/O = 1.26 ± 0.15) in the first few nanometers of the surface obtained by XPS analysis, the position of the PL maximum at 2.88 eV (430 nm), and the non-equilibrium synthesis conditions that favour the formation of Zn-rich ZnO. A correlation between zinc interstitials and the presence of violet luminescence was confirmed by electron paramagnetic resonance (EPR) measurements for ZnO samples with a zinc excess.[12,13,15] This correlation between the violet photoluminescence signal and the EPR signals is summarized as follows: two pairs of signals (2.88 eV with g = 1.956 and 2.80 eV with g = 1.960) were associated with the same type of defect (Zn_i), but they were localized in slightly different crystallographic environments.[12,13] Based on these results, in oxygen deficient zinc oxide $ZnO_{0.85}$ thin films, the PL peaks located around 2.9 eV could be assigned to the Zn_i defect. Moreover, a Zn/O ratio of 1.18 ± 0.1 across the entire thickness of the oxygen deficient zinc oxide thin films was provided by RBS measurements. The studies of Zhang *et al.*[12,13] correlate the observed PL and EPR fingerprints with the presence of specific defects that produce distinct PL emissions, ranging from violet to green and yellow. For example, a significant decrease in violet photoluminescence intensity upon interaction with oxygen indicates that the underlying zinc interstitial defect becomes optically inactive.

These results are consistent with other reports.[15,16,46] The blue luminescence of the ZnO nanoparticles with emission wavelengths of 415, 440, 455 and 488 nm was investigated and attributed to transitions from the Zn_i and extended Zn_i states to the valence band.[15] The highly non-equilibrium synthesis conditions, including laser ablation in liquid and zinc-rich annealing, produced a high concentration of zinc interstitial defects, which were the predominant defects in the as-prepared samples and also confirmed by EPR measurements.[15]

The ZnO nanostructures fabricated by atomic layer deposition with a higher density of zinc interstitial defects compared to oxygen vacancy defects, also showed blue emission peaks in the photoluminescence spectra in the 400–437 nm region (3.10–2.83 eV), which were assigned to transitions from the zinc interstitial defect states (3.10–3.04 eV) and their extended states to the valence band of ZnO (2.86–2.83 eV).[46] The zinc interstitial defects were found to be less efficient for photocatalysis compared to the oxygen vacancy defects, due to the greater accessibility and "double effect" of the oxygen vacancy defects in trapping both holes and electrons and delaying recombination.[46]

This type of photoluminescence emission was also observed for metallic zinc nanostructures during the transition from the bulk to the nanoscale regime.[14] Both emission peaks at 3.0 and 2.9 eV were assigned to the relaxation of electrons excited *via* the 3d–sp interband transition in metallic zinc, while the emission at 2.7 eV was attributed to the relaxation of electrons excited *via* the sp–sp interband transition.[14]

For a moderate oxygen-deficiency in ZnO_{1-x} nanosheets (gray color), only yellow-green photoluminescence emission was observed, which is explained by singly ionized surface oxygen vacancies that were not present in the stoichiometric, defect-free ZnO sample.[47] These ZnO_{1-x} nanosheets presented the light absorption into the visible region, and excellent photocatalytic activity compared to stoichiometric ZnO.[47]

Regarding the quenching of violet and blue PL, few approaches were employed. As the degree of oxygen deficiency

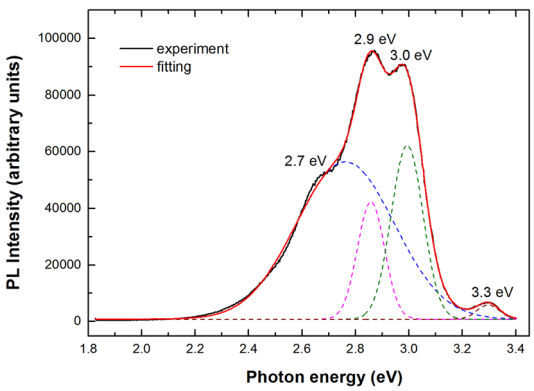

Fig. 2 Photoluminescence spectrum of a black amorphous $ZnO_{0.85}$ thin film grown on a c-cut single crystal sapphire substrate at 300 °C in argon at a pressure of 9×10^{-3} mbar (black line) together with its envelope (red line) and four Gaussian (dashed line) fitting.

in the ZnO thin films decreases (the films turn from a dark color to gray), the violet and blue PL emission diminishes.[47] The intensity of violet photoluminescence emission presents a reactivity towards oxygen, either enhancing the formation of Zn_i defects and violet emission in low oxygen partial pressure or becoming optically inactive centers under rich oxygen pressure.[12,13] Low-temperature annealing increases the concentration of zinc interstitial defects, enhancing the blue emissions, while high-temperature annealing leads to the diffusion of zinc interstitial defects and quenching of the blue emissions.[15]

However, the variations in the exact peak positions and relative intensities of the violet/blue PL suggest that the zinc interstitial defect concentration is influenced by specific parameters related to the growth technique, deposition temperature, and post-deposition treatments.[12–16,46–49] This could be due to differences in growth kinetics, energy of deposited species, and the ability to control stoichiometry during zinc oxide film formation. For example, the PED technique involves high-energy species that may create more point defects and a precise control of the oxygen deficiency. Therefore, the film composition, in fact the degree of oxygen deficiency, is a key parameter in determining the PL signatures associated with Zn interstitials. However, the lack of consistent reporting and systematic variation of parameters across studies makes it challenging to establish quantitative relationships between processing conditions and PL signatures.

Since PL measurements are typically performed on crystalline ZnO thin films,[17,51] the structure of $ZnO_{0.85}$ thin films was investigated by XRD and compared with that of epitaxial and stoichiometric ZnO thin films. The epitaxial stoichiometric ZnO thin films were grown on a c-cut single crystal sapphire substrate at 500 °C by PED under a higher argon pressure (2×10^{-2} mbar) than that used in this work (9×10^{-3} mbar).

A comparison between the photoluminescence spectra of an oxygen deficient $ZnO_{0.85}$ thin film (blue solid line) and an epitaxial stoichiometric ZnO thin film (black dashed line) is shown in Fig. 3a. Both PL spectra are normalized to the maximum value. These PL spectra reveal substantial differences in their emission bands primarily due to differences in contributions from defect-related emissions.

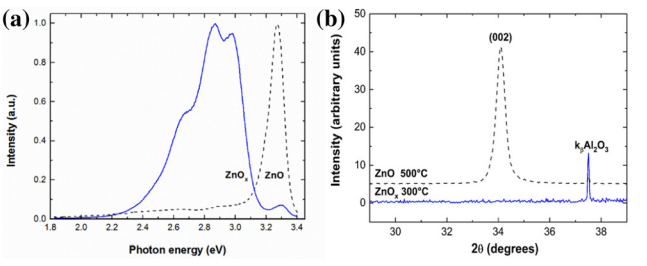

Fig. 3 (a) Photoluminescence spectra and (b) θ–2θ diffraction patterns of a $ZnO_{0.85}$ thin film grown on a c-cut single crystal substrate at 300 °C and an argon pressure of 9×10^{-3} mbar (blue solid line) and of an epitaxial stoichiometric ZnO thin film grown on a c-cut sapphire substrate at 500 °C under 2×10^{-2} mbar argon pressure (dashed line).

The crystalline structure of the oxygen deficient $ZnO_{0.85}$ thin film was examined by XRD and the corresponding θ–2θ pattern is plotted as shown in Fig. 3b (continuous line). Peaks of the ZnO würtzite structure or metallic zinc with a hexagonal crystal structure were not detected, suggesting that the film can be considered nanocrystalline or amorphous. This result is rather unexpected because of the high propensity of zinc oxide to crystallize at low temperatures, but it is consistent with the film non-stoichiometry that appears as a key factor for the amorphous ZnO_x films.[11,50]

The θ–2θ pattern for the epitaxial and stoichiometric ZnO thin film is also plotted as shown in Fig. 3b (black dashed line), showing the characteristic (002) reflection peak of the ZnO würtzite structure. Details about the epitaxy of ZnO thin films grown on a c-cut single crystal sapphire substrate (including pole figures) are given elsewhere.[20]

The epitaxial and stoichiometric ZnO transparent films present an intense NBE emission at 3.3 eV, close to the bandgap of ZnO, that dominates the spectrum. This indicates that the majority of electrons recombine radiatively with holes at or near the conduction band without being trapped by deep-level defects.[17,51] The sharp and intense NBE emission is typically related to a higher degree of crystallinity of ZnO (epitaxy) with respect to the low intensity and broad NBE emission of the oxygen deficient $ZnO_{0.85}$ thin films.

The typical PL signal associated with oxygen vacancies at approximately 2.2 eV, a native point defect of zinc oxide (ZnO),[52] was not observed in oxygen-deficient ZnO thin films (Fig. 2), nor in stoichiometric, epitaxial ZnO thin films grown on a c-cut sapphire single crystal substrate at 500 °C under an argon pressure of 2×10^{-2} mbar (Fig. 3a, dashed line). The oxygen deficiency in black zinc oxide films differs significantly from the ideal ZnO stoichiometry, resulting in a lower-than-expected number of oxygen atoms (about 15% missing). In contrast, oxygen vacancies are a type of point defect in a crystal lattice where an oxygen atom is missing from its regular position, but in our case, the films are amorphous. By analogy with crystalline films, oxygen vacancies are considered point defects that impact the film properties like PL. However, to what extent the structure and properties of point defects in amorphous solids are similar to those in the crystalline phase is still debated.[53]

Although oxygen vacancies are the native point defects of ZnO,[52] XPS and PL measurements revealed no oxygen vacancies in many crystalline ZnO thin films, proving that the film growth is essential for PL properties.[52,54,55] For example, the XPS ZnLMM and O 1s spectra of polycrystalline ZnO thin films grown on quartz substrates by sol–gel spin coating have revealed that zinc interstitials and zinc vacancies dominate over oxygen vacancies as a function of post-annealing temperature, modifying the features of the PL spectra in the visible region.[54] Moreover, the EPR measurements indicate the presence of zinc vacancies and zinc interstitials for high annealing temperatures (400 °C and 500 °C) and only zinc vacancies for 300 °C.[54] Zinc interstitials were introduced by decreasing the oxygen pressure during the growth of Al doped ZnO epitaxial

thin films on c-cut and r-cut sapphire substrates.[55] Due to the fact that the Al–O bond strength (511 ± 3 kJ mol^{-1}) and ionization tendency are larger than those of Zn–O (159 ± 4 kJ mol^{-1}), the Al dopant prefers to bind with oxygen; hence, the Al doping suppresses the formation of oxygen vacancies during film growth.[55] By analogy, and taking into account the amorphous nature of the films and the absence of dopants, the formation of oxygen vacancies is not ensured by a number of oxygen atoms smaller than that required by the stoichiometric composition.

Amorphous ZnO films do not exhibit the sharp near-band edge emission due to the lack of long-range order, which inhibits the formation of free and bound excitons that contribute to the sharp ultraviolet emission as observed in crystalline films. As a result, the PL spectrum of the amorphous $ZnO_{0.85}$ film is dominated by defect-related emissions.[12–16,41,46–49]

The advantages of PED over PLD and sputtering for achieving high oxygen deficiency are related to the control of oxygen incorporation in the oxide thin films. The defect-related PL emission is related to the degree of oxygen deficiency in the $ZnO_{0.85}$ thin films. The variation of the amount of oxygen, from a highly oxygen deficient value (x = 0.85) to an almost stoichiometric value (x = 1), depends on the PED growth conditions (argon pressure, substrate temperature and deposition rate) that is related to the kinetic energy of the species arriving at the substrate.[11] For example, the growth of the amorphous $ZnO_{0.85}$ thin film is associated with high kinetic energies and a deposition rate more than 2.5 times higher with respect to that for growing stoichiometric and crystalline ZnO films. Thus, in amorphous ZnO films, the absence of a well-defined crystal lattice leads to the formation of a large number of localized defect states within the bandgap, the efficiency of exciton recombination is reduced and the violet/blue emission becomes more prominent.

In the case of amorphous zinc–indium–tin oxide thin films, coordination numbers and bond lengths were obtained from grazing-incidence X-ray pair-distribution function (PDF) analysis for short-range ordering using high-energy synchrotron X-rays, and the results were in agreement with theoretical simulations.[56] The Zn–O bond length and coordination number decreased by ~0.1 Å and ~1 (fourfold coordination), respectively, in amorphous zinc–indium–tin films, compared to its crystalline counterpart.[56] The decrease in Zn–O bond length with decreasing coordination is consistent with theoretical studies on amorphous and stoichiometric ZnO.[57] A Monte Carlo study related to the grain growth kinetics in two-phase nanostructured films, *i.e.* nanocrystallites embedded in an amorphous matrix, proved that an amorphous matrix could significantly hinder the grain growth kinetics, resulting in a reduction in grain size or a decrease in the grain growth exponent when compared with grain growth behaviour observed in epitaxial and polycrystalline films.[58] Therefore, the amorphous zinc oxide film acts as a barrier, thus inhibiting the movement of grain boundaries and slowing down the process of grain growth.[58]

Since the value of the binding energy of the Zn $2p_{3/2}$ zinc oxide peak (1021.7 eV) is very close to the binding energy of the Zn metal peak (1021.4 eV),[59] the study of zinc chemistry by X-ray photoelectron spectroscopy is typically carried out by analyzing the shape and energy position of the most intense Zn $L_3M_{45}M_{45}$ (Zn LMM) Auger line,[60] in the absence of significant Zn 2p level shifts. High resolution core-level spectra of Zn 2p, Zn LMM, Zn 3p and O 1s are presented in Fig. 4a–d.

The surface of the black amorphous $ZnO_{0.85}$ thin film exhibits Zn 2p peaks at 1022.1 eV and 1045.1 eV, Zn 3p peaks at ~89 and 91.7 eV and an O 1s peak at 530.7 eV, which are consistent with the typical XPS spectra of ZnO.[59–61]

In the Zn LMM Auger transition, the core hole in the Zn $2p_{3/2}$ level (L_3) is filled by an electron decayed from the Zn 3d level (M_{45}) and the energy difference is used to emit an electron from the Zn 3d level (M_{45}). The recorded Zn LMM spectrum is shown in Fig. 4b, presenting a main peak at 498.6 eV and a shoulder at ~495 eV, being the signature of zinc oxide. In the case of Zn metal, both a significant shift towards a lower binding energy (around few eV) and a narrower Zn LMM profile should be observed.[60]

To confirm the oxidation state, the modified Auger parameter, defined as the sum of the binding energy of the Zn $2p_{3/2}$ core-level photoelectron line and the kinetic energy of the Zn $L_3M_{45}M_{45}$ Auger-transition line, was calculated.[11,50,60–63] The 2010.1 eV value obtained using the main peak confirms the Zn^{2+} valence state. A value of about 2013.7 eV using the shoulder at ~495 eV is close to the signature of the Zn (Zn^0) metal.[60–63] In this case, a very slight presence of the metal Zn in $ZnO_{0.85}$ thin films could not be excluded,[18,50,59,60] but the high oxygen deficiency is not enough to change the shape and shift the Zn LMM spectrum.

The luminescence mechanism of the green light emission from a ZnO thin film was associated primarily with oxygen vacancies in a study where the photoluminescence measurements were correlated with XPS investigations.[52] The Zn LMM peaks of ZnO thin films annealed at various temperatures did not show a shoulder as in our case.[52,62] The α values of ZnO films annealed at 600–800 °C were determined to be approximately 2011 eV, while that of the film annealed at 900 °C was approximately 2009.6 eV.[52]

Since Zn 2p is a surface sensitive peak revealing the chemical composition of the $ZnO_{0.85}$ thin film up to 2–3 nm, the Zn 3p XPS spectrum (Fig. 4c), which is a doublet peak with 2.7 eV splitting, probes deeper twice in the film.

The O 1s spectrum was deconvoluted into two component peaks (Fig. 4d). The first peak at 530.7 eV, assigned to oxygen (2−), is narrow (FWHM of 1.27 eV), indicating a more defective surface state for the black zinc oxide films, as already reported.[12–16,46–50] The overlapping component at higher binding energy (532.5 eV) is attributed to the surface organic contaminants.[46–50]

Resistivity, carrier density and mobility of amorphous $ZnO_{0.85}$ thin films were measured by the Hall effect at room temperature. The black zinc oxide thin films are n-type and have the highest value of carrier density among those recorded for the films grown by PED (6.55×10^{20} cm^{-3}), being highly degenerate semiconductors with respect to the Mott critical

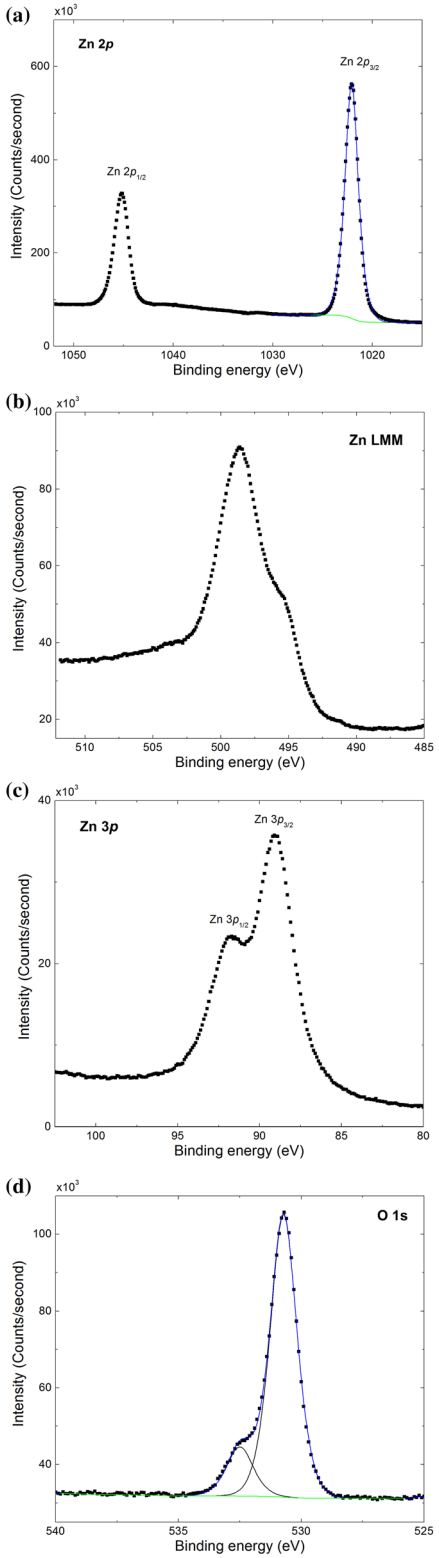

Fig. 4 High resolution core-level spectra of an amorphous $ZnO_{0.85}$ thin film grown on a c-cut single crystal substrate at 300 °C and an argon pressure of 9×10^{-3} mbar: (a) Zn 2p, (b) Zn LMM, (c) Zn 3p and (d) O 1s.

carrier density (for ZnO ~ 10^{19} cm^{-3} [11]). A resistivity of 1.129 10^{-2} Ω cm and an electron mobility of 1.27 V cm^{-2} s^{-1} were obtained. The high carrier concentration, as measured by the Hall effect, could be correlated with an increased density of defects in ZnO such as oxygen vacancies and zinc interstitials but without making a distinction between them.[3] These defects act as donor states, providing free electrons that contribute to the n-type high conductivity of $ZnO_{0.85}$ films.

In the case of degenerated crystalline ZnO thin films (carrier density higher than the Mott critical carrier density[11,55]), ionized impurity scattering and grain boundary scattering represent the predominant carrier scattering processes.[55] In the case where grain boundary scattering is found to be dominant, mobility increases with increasing temperature; when the ionized impurity scattering is dominant, mobility does not depend on temperature,[55] as already observed for doped stoichiometric ZnO thin films grown by PED.[20]

For amorphous oxygen-deficient zinc oxide thin films, the temperature-dependent resistivity showed a semiconducting-like shape with a slight increase between 300 K and 5 K, similar to that previously measured.[11] This feature, in correlation with the high value of carrier density (6.55×10^{20} cm^{-3}) and amorphous structural disorder, corresponds to large disordered metallic-like oxide films and was explained by the quantum corrections to the conductivity model.[11]

Although electrical transport models have been transferred from crystals to amorphous solids, this correspondence still remains to be elucidated by experimental and theoretical studies.[53] In fact, many studies assume that oxygen vacancies in amorphous films can reversibly capture and release electrons due to the fact that the electrical and optical properties of polycrystalline and amorphous oxide films are qualitatively similar for the same film composition.[53] In our case, the amorphous zinc oxide films do not present the same composition as the polycrystalline or epitaxial thin films counterparts. As an example, the stoichiometric, polycrystalline and transparent ZnO thin films grown by PED present a resistivity about ten times lower, a carrier density two times lower and an electron mobility five times higher than those corresponding to the amorphous black zinc oxide thin film.[11] In the case of zinc–indium–tin oxide amorphous films, it has been determined that the valence electrons associated with under-coordinated fourfold In and Sn ions represent the main charge transport mechanism for conductivity, while Zn remains fully coordinated (4-fold oxygen atoms).[56]

The lack of periodicity and irregularities of bonds in amorphous transparent conducting oxides contribute to the formation of localized defect states near the band edges, thus leading to electron trapping, carrier scattering and subgap absorption as demonstrated by simulations.[43,56,57] Hence, in oxygen deficient $ZnO_{0.85}$ thin films, not only zinc interstitials and oxygen vacancies but also few Zn metal clusters could behave as electron scattering centers, contribute to electron trapping, and generate subgap states,[43,50,64–69] which could explain the low value of electron mobility (1.27 V cm^{-2} s^{-1}) of $ZnO_{0.85}$ films. In addition, X-ray absorption near edge structure

(XANES) studies proved that the electron mean free path contributing to the electrical conduction in amorphous ZnO films is rather limited compared to crystalline ZnO films due to the structural disorder.[70] However, the analogy between the defect scattering from grain-boundary effects of defects in crystalline and amorphous oxides needs further investigation.

D. Conclusions

Oxygen deficiency in ZnO thin films is a key factor in determining their optical and electrical properties. Film growth methods such as PED can be tailored to control the oxygen deficiency concentration, thereby allowing the synthesis of ZnO films with desired properties for specific applications. The measurement of oxygen deficiency in $ZnO_{0.85}$ thin films is a critical aspect of understanding their electronic and optical behavior.

The presence of high oxygen deficiency leads to darkened or black films by introducing deep-level defect states in the bandgap that absorb visible light with a high electron concentration in the conduction band. Techniques such as XRD, XPS and Hall effect measurements, combined with optical characterization through PL, allowed for complementary insights into the composition and defect structure of ZnO films.

The PL spectra show distinct peaks corresponding to the energy levels associated with Zn_i defects and their extended states, indicating their role in the luminescence properties of the material. Amorphous ZnO films show broad, defect-induced emissions in the visible spectrum and lack the sharp UV emission peak associated with free and bound excitons.

The ability to control oxygen deficiency is crucial for optimizing ZnO thin films for applications. Black ZnO thin films, which exhibit enhanced absorption in the visible and near-infrared regions due to large oxygen deficiency and high carrier concentration, could be used for solar absorbers and photocatalysis. Amorphous ZnO films are attractive for applications that require flexible or low-cost deposition methods. Interfacial structures can be made for zinc metal anodes in aqueous media for applications in zinc metal batteries,[26] as these films possess the required moderate adsorption energy, strong desolvation ability and enhanced hydrophilicity.[26,27] As the demand for ZnO-based devices continues to grow, the ability to control and engineer photoluminescence through deposition techniques and post-processing treatments will play a pivotal role in advancing the performance and functionality of ZnO-based technologies.

Author contributions

M. Nistor: conceptualization (lead), formal analysis (lead), investigation (lead), writing – original draft (lead), visualization (equal), and writing – review and editing (lead). F. Gherendi: investigation (equal) and review and editing (supporting); D. Dobrin: investigation (equal) and review and editing (supporting); J. Perrière: conceptualization (supporting), investigation (equal), and writing – review and editing (supporting).

Conflicts of interest

There are no conflicts of interest to declare.

Data availability

The data that support the findings of this study are available from the corresponding author upon reasonable request.

Acknowledgements

M. N., D. D., and F. G. acknowledge the Romanian Ministry of Education and Research under the National Core Program LAPLAS VII – contract no. 30N/2023. The agreement on cooperation between INFLPR, Măgurele and INSP, Université Pierre et Marie Curie-Paris 6 (now Sorbonne University) is acknowledged. The RBS measurements were carried out within the cooperative structure around SAFIR (Sorbonne University). Dr I. Enculescu (National Institute for Materials Physics) is acknowledged for photoluminescence measurements.

References

1 J. Gu, F. Duan, S. Liu, W. Cha and J. Lu, *Chem. Rev.*, 2024, **124**, 1247–1287.
2 M. Nistor, J. Perrière, C. Hebert and W. Seiler, *J. Phys.: Condens. Matter*, 2010, **22**, 045006.
3 L. Schmidt-Mende and J. L. MacManus-Driscoll, *Mater. Today*, 2007, **10**, 40–48.
4 S. Varnagiris, M. Urbonavicius, S. Tuckute and M. Lelis, *Thin Solid Films*, 2021, **738**, 138967.
5 A. Badreldin, A. Abdel-Wahab and P. B. Balbuena, *ACS Appl. Energy Mater.*, 2020, **3**, 10590–10599.
6 Y. Chen, P. Schneider, B.-J. Liu, S. Borodin, B. Ren and A. Erbe, *Phys. Chem. Chem. Phys.*, 2013, **15**, 9812–9822.
7 J. Zuo and A. Erbe, *Phys. Chem. Chem. Phys.*, 2010, **12**, 11467.
8 M. Krzywiecki, L. Grządziel, A. Sarfraz, D. Iqbal, A. Szwajca and A. Erbe, *Phys. Chem. Chem. Phys.*, 2015, **17**, 10004–10013.
9 K. Mika, K. Syrek, T. Uchacz, G. D. Sulka and L. Zaraska, *Electrochim. Acta*, 2022, **414**, 140176.
10 K. Mika, R. P. Socha, P. Nyga, E. Wiercigroch, K. Małek, M. Jarosz, T. Uchacz, G. D. Sulka and L. Zaraska, *Electrochim. Acta*, 2019, **305**, 349–359.
11 M. Nistor, F. Gherendi, D. Dobrin and J. Perrière, *J. Appl. Phys.*, 2022, **132**, 225705.
12 M. Zhang, F. Averseng, F. Haque, P. Borghetti, J.-M. Krafft, B. Baptiste, G. Costentin and S. Stankic, *Nanoscale*, 2019, **11**, 5102–5115.

13 M. Zhang, F. Averseng, J.-M. Krafft, P. Borghetti, G. Costentin and S. Stankic, *J. Phys. Chem. C*, 2020, **124**, 12696–12704.
14 N. T. Mai, T. T. Thuy, D. M. Mott and S. Maenosono, *CrystEngComm*, 2013, **15**, 6606.
15 H. Zeng, G. Duan, Y. Li, S. Yang, X. Xu and W. Cai, *Adv. Funct. Mater.*, 2010, **20**, 561–572.
16 J.-H. Lin, R. A. Patil, R. S. Devan, Z.-A. Liu, Y.-P. Wang, C.-H. Ho, Y. Liou and Y.-R. Ma, *Sci. Rep.*, 2014, **4**, 6967.
17 X. L. Wu, G. G. Siu, C. L. Fu and H. C. Ong, *Appl. Phys. Lett.*, 2001, **78**, 2285–2287.
18 C. Cachoncinlle, E. Millon, X. Portier, C. Hebert, J. Perrière and M. Nistor, *Appl. Phys. A*, 2022, **128**, 530.
19 J. Perrière, C. Hebert, N. Jedrecy, W. Seiler, O. Zanellato, X. Portier, R. Perez-Casero, E. Millon and M. Nistor, *J. Appl. Phys.*, 2014, **116**, 123502.
20 M. Nistor, F. Gherendi and J. Perrière, *Opt. Mater.*, 2022, **126**, 112154.
21 H.-C. Tang, J. Kim, H. Hiramatsu, H. Hosono and T. Kamiya, *J. Ceram. Soc. Jpn.*, 2015, **123**, 523–526.
22 M. Zubkins, J. Gabrusenoks, G. Chikvaidze, I. Aulika, J. Butikova, R. Kalendarev and L. Bikse, *J. Appl. Phys.*, 2020, **128**, 215303.
23 J. Bruncko, A. Vincze, M. Netrvalova, P. Šutta, D. Hasko and M. Michalka, *Thin Solid Films*, 2011, **520**, 866–870.
24 N. Asakuma, H. Hirashima, T. Fukui, M. Toki, K. Awazu and H. Imai, *Jpn. J. Appl. Phys.*, 2002, **41**, 3909–3915.
25 J. Tellier, D. Kuščer, B. Malič, J. Cilenšek, M. Škarabot, J. Kovač, G. Gonçalves, I. Muševič and M. Kosec, *Thin Solid Films*, 2010, **518**, 5134–5139.
26 W. Lu, H. Jiang, Z. Wei, N. Chen, Y. Wang, D. Zhang and F. Du, *Nano Lett.*, 2024, **24**, 2337–2344.
27 Z. Zhao, R. Wang, C. Peng, W. Chen, T. Wu, B. Hu, W. Weng, Y. Yao, J. Zeng, Z. Chen, P. Liu, Y. Liu, G. Li, J. Guo, H. Lu and Z. Guo, *Nat. Commun.*, 2021, **12**, 6606.
28 S. Zhou, Y. Wang, H. Lu, Y. Zhang, C. Fu, I. Usman, Z. Liu, M. Feng, G. Fang, X. Cao, S. Liang and A. Pan, *Adv. Funct. Mater.*, 2021, **31**, 2104361.
29 H. Akazawa, *J. Vac. Sci. Technol., A*, 2021, **39**, 033411.
30 H. Akazawa, *J. Vac. Sci. Technol., A*, 2021, **39**, 053401.
31 J. Clatot, M. Nistor and A. Rougier, *Thin Solid Films*, 2013, **531**, 197–202.
32 C. Faure, J. Clatot, L. Teulé-Gay, G. Campet, C. Labrugère, M. Nistor and A. Rougier, *Thin Solid Films*, 2012, **524**, 151–156.
33 Ts. Naydenova, P. Atanasov, M. Koleva, N. Nedialkov, J. Perriere, D. Defourneau, H. Fukuoka, M. Obara, Ch. Baumgart, Sh. Zhou and H. Schmidt, *Thin Solid Films*, 2010, **518**, 5505–5508.
34 V. Craciun, R. K. Singh, J. Perriere, J. Spear and D. Craciun, *J. Electrochem. Soc.*, 2000, **147**, 1077.
35 V. Craciun, J. Perriere, N. Bassim, R. K. Singh, D. Craciun and J. Spear, *Appl. Phys. A*, 1999, **69**, S531–S533.
36 M. Nistor, F. Gherendi and J. Perrière, *Mater. Sci. Semicond. Process.*, 2018, **88**, 45–50.
37 P. Graziosi, M. Prezioso, A. Gambardella, C. Kitts, R. K. Rakshit, A. Riminucci, I. Bergenti, F. Borgatti, C. Pernechele, M. Solzi, D. Pullini, D. Busquets-Mataix and V. A. Dediu, *Thin Solid Films*, 2013, **534**, 83–89.
38 D. Dobrin, I. Burducea, D. Iancu, C. Burducea, F. Gherendi and M. Nistor, *Appl. Surf. Sci.*, 2024, **657**, 159757.
39 R. Comes, M. Gu, M. Khokhlov, H. Liu, J. Lu and S. A. Wolf, *J. Appl. Phys.*, 2013, **113**, 023303.
40 S. Tricot, C. Boulmer-Leborgne, M. Nistor, E. Millon and J. Perrière, *J. Phys. D: Appl. Phys.*, 2008, **41**, 175205.
41 P. H. Quang, N. D. Sang and D. Q. Ngoc, *Thin Solid Films*, 2012, **520**, 6455–6458.
42 L. R. Doolittle, *Nucl. Instrum. Methods Phys. Res., Sect. B*, 1985, **9**, 344–351.
43 J. E. Medvedeva, E. Caputa-Hatley and I. Zhuravlev, *Phys. Rev. Mater.*, 2022, **6**, 02560144.
44 R. Gomez-San Roman, R. P. Casero, C. Maréchal, J. P. Enard and J. Perrière, *J. Appl. Phys.*, 1996, **80**, 1787–1793.
45 T. Wijnands, E. P. Houwman, G. Koster, G. Rijnders and M. Huijben, *Phys. Rev. Mater.*, 2020, **4**, 103803.
46 T. F. Kayaci, S. Vempati, I. Donmez, N. Biyikli and T. Uyar, *Nanoscale*, 2014, **6**, 10224–10234.
47 H.-L. Guo, Q. Zhu, X.-L. Wu, Y.-F. Jiang, X. Xie and A.-W. Xu, *Nanoscale*, 2015, **7**, 7216–7223.
48 S. Pramanik, S. Das, R. Karmakar, Sk. Irsad Ali, S. Mukherjee, S. Dey, A. C. Mandal, A. K. Meikap and P. K. Kuiri, *J. Lumin.*, 2023, **257**, 119746.
49 H.-S. Chou, K.-D. Yang, S.-H. Xiao, R. A. Patil, C.-C. Lai, W.-C. V. Yeh, C.-H. Ho, Y. Liou and Y.-R. Ma, *Nanoscale*, 2019, **11**, 13385–13396.
50 E. A. Redekop, T. Cordero-Lanzac, D. Salusso, A. Pokle, S. Oien-Odegaard, M. F. Sunding, S. Diplas, C. Negri, E. Borfecchia, S. Bordiga and U. Olsbye, *Chem. Mater.*, 2023, **35**, 10434–10445.
51 X. L. Wu, G. G. Siu, C. L. Fu and H. C. Ong, *Appl. Phys. Lett.*, 2001, **78**, 2285–2287.
52 P.-T. Hsieh, Y.-C. Chen, K.-S. Kao and C.-M. Wang, *Appl. Phys. A*, 2007, **90**, 317–321.
53 J. Strand and A. L. Shluger, *Adv. Sci.*, 2024, **11**, 2306243.
54 M. Podia and A. K. Tripathi, *J. Lumin.*, 2025, **280**, 121083.
55 Y. Komatsubara, T. Ishibe, S. Kozuki, K. Sato, E. Kobayashi, Y. Yamashita, N. Naruse, Y. Mera, Y. Shiratsuchi, J. Ohe, M. Uenuma and Y. Nakamura, *ACS Appl. Mater. Interfaces*, 2025, **17**, 46276–46284.
56 G. B. González, C. J. Benmore, J. E. Medvedeva, J. S. Okasinski, C. Riegger, O. Medina, M. M. Stulajter, T. Bsaibes, G. Cardenas, S. Cone, K. Edlund, M. Osorio, T. Holmes, I. Zhuravlev, B. Bhattarai, D. B. Buchholz and R. P. H. Chang, *J. Appl. Phys.*, 2025, **137**, 115104.
57 J. E. Medvedeva, B. Bhattarai and D. B. Buchholz, in *Amorphous Oxide Semiconductors*, ed. H. Hosono and H. Kumomi, Wiley, 1st edn, 2022, pp. 31–72.
58 Z.-J. Liu and Y. G. Shen, *Acta Mater.*, 2004, **52**, 729–736.

59 M. C. Biesinger, B. P. Payne, A. P. Grosvenor, L. W. M. Lau, A. R. Gerson and R. St. C. Smart, *Appl. Surf. Sci.*, 2011, **257**, 2717–2730.
60 C. Morales, A. Black, F. J. Urbanos, D. Granados, J. Méndez, A. Del Campo, F. Yubero and L. Soriano, *Adv. Mater. Interfaces*, 2019, **6**, 1801689.
61 Y. Cao, J. Luo, W. Huang, Y. Ling, J. Zhu, W.-X. Li, F. Yang and X. Bao, *J. Chem. Phys.*, 2020, **152**, 074714.
62 P. Wendel, S. Periyannan, W. Jaegermann and A. Klein, *Phys. Rev. Mater.*, 2020, **4**, 084604.
63 G. Moretti, *Surf. Sci.*, 2013, **618**, 3–11.
64 W. Körner, P. Gumbsch and C. Elsässer, *Phys. Rev. B: Condens. Matter Mater. Phys.*, 2012, **86**, 165210.
65 Z. Wang, J. Byun, S. Lee, J. Seo, B. Park, J. C. Kim, H. Y. Jeong, J. Bang, J. Lee and S. H. Oh, *Nat. Commun.*, 2022, **13**, 5616.
66 J. Wang, Z. Wang, B. Huang, Y. Ma, Y. Liu, X. Qin, X. Zhang and Y. Dai, *ACS Appl. Mater. Interfaces*, 2012, **4**, 4024–4030.
67 M. Bizarro, M. Ballesteros-Balbuena, V. H. Castrejón-Sánchez, A. Hernández-Gordillo and M. Camacho-López, *Micro Nanostruct.*, 2025, **199**, 208070.
68 E. G. Barbagiovanni, R. Reitano, G. Franzò, V. Strano, A. Terrasi and S. Mirabella, *Nanoscale*, 2016, **8**, 995–1006.
69 Q. Guo, Y. Dai and Y. Qi, *J. Chem. Phys.*, 2024, **161**, 084701.
70 D.-Y. Cho, J. H. Kim and C. S. Hwang, *Appl. Phys. Lett.*, 2011, **98**, 222108.